Investigating the effect of retained austenite and residual stress on rolling contact fatigue of carburized steel with XFEM and experimental approaches

by

George Theng Ching Ooi

A thesis submitted to the graduate faculty

in partial fulfillment of the requirements for the degree of

MASTER OF SCIENCE

Major: Mechanical Engineering

Program of Study Committee:
Sriram Sundararajan, Major Professor
Adarsh Krishnamurthy
Wei Hong

The student author, whose presentation of the scholarship herein was approved by the program of study committee, is solely responsible for the content of this thesis. The Graduate College will ensure this thesis is globally accessible and will not permit alterations after a degree is conferred.

Iowa State University

Ames, Iowa

2018

TABLE OF CONTENTS

Page

LIST OF FIGURES

Page

LIST OF TABLES

ACKNOWLEDGMENTS

I would like to take this opportunity to thank my major professor, Dr. Sundararajan for his guidance and the opportunity to be part of his research group. Without his support, I would not be able to complete my research project. I would also like to express my gratitude to my committee members, Dr. Krishnamurthy and Dr. Hong for their advices and research supports in computational works and Finite Element Methods. I would also like to thank Sougata Roy who has been providing feedbacks and suggestions in my research project. In addition, I also want to offer my appreciation to those who have been encouraging and praying for me throughout my studies. Last but not least, I would like to thank my parents and my family who have been always encouraging and supporting me to further advance my education in the United States.

ABSTRACT

In this study, the effects of retained austenite (RA) and residual stress on rolling contact fatigue (RCF) of carburized AISI 8620 steel were investigated through modeling and experiments. In modeling, a two-dimensional finite element RCF model was developed to examine the crack propagation and fatigue life of carburized AISI 8620 steel. An extended finite element method (XFEM) was used to initiate and propagate the cracks in the model. A Voronoi tessellation was randomly generated to simulate the randomness of the microstructures in steel. The cracks were initiated on the grain boundaries of a Voronoi cell prior to the simulations at different locations in the RCF model. The RCF life of the samples was determined by rolling contact fatigue tests. The results in both simulations and experiments showed that the higher level of RA and compressive residual stress achieved improved RCF life through mitigation of crack propagation. The effect of increased RA led to significant improvement on RCF life as compared to increased in compressive residual stress.

CHAPTER 1. INTRODUCTION

Background and Motivation

Rolling element bearing is a machine component that is specially designed to constrain relative rotation movement, withstand high pressure forces and reduce friction between moving parts. The application of bearings is widely used in automobiles, machineries, and home appliances. Improving the reliability and efficiency of rolling element bearings has became a crucial task in industries as this directly impacts the cost and quality of the systems and products. One major failure in rolling element bearing is rolling contact fatigue (RCF). RCF is commonly aroused in rolling element bearings due to repeated cyclic loading of the materials that generates high local Hertzian pressures, leading to micro-plastic deformation, localized damage, possibly crack initiation and propagation which eventually leads to spalling and pitting. Spalling is usually referred to macropitting with deeper pit whereas smaller and shallower pit is called micropitting [1]. Many studies have been conducted to identify the root causes of these failure modes. Some researchers have shown that the effect of the maximum normal stress or alternating shear stress under rolling contact below the surface can initiate subsurface cracks which lead to spalling [2-6]. On the other hand, micropitting is observed as a surface initiated phenomenon [7]. Surface initiated crack can occur due to improper use of lubricant or flaw on surface and improper surface finishing. Since modern bearing steels are clean and well lubricated, spalling is more likely to happen due to subsurface initiated cracks.

As technology advances, engineers and scientists have developed different statistical and probabilistic models to estimate the fatigue life through experiments and simulations [3].

However, the phenomenon and physical mechanism of RCF has not been fully understood yet. RCF is a complicated fatigue failure problem because of several external and internal factors that contribute to the complexity and uncertainty of RCF. Studies have shown that these parameters such as retained austenite [8], amount of residual stress [9], heat treatment techniques [10], and type of lubricants [11] influence the RCF life. In order to improve fatigue life, heat treatment is commonly used to induce residual stress and retained austenite in steels [12]. It is well-known that inducing compressive residual stress in steel provides positive effects on fatigue life [13]. Retained austenite is austenite that retains in steel and does not transform into martensite upon quenching. Several studies have showed that the effect of retained austenite and compressive residual stress in steel reduces the probability of cracks initiation and propagation, and thus prolongs the RCF life of rolling element bearings and gears [14, 15]. However, some studies have found that austenite would decrease fatigue life [16, 17].

While the literature typically accounts for the individual effect of retained austenite or residual stress, the coupled effects of retained austenite and residual stress are extremely important [9, 15, 16, 18-21]. The amount of residual stress induced in the material may depend on the amount of retained austenite [8, 22]. According to [23], increasing the level of retained austenite could decrease the amount of residual stress in steel due to lesser transformation from austenite to martensite upon quenching which accompanied with the volume expansion that induced the compressive residual stress. However, in previously reported experimental studies [10, 24], the correlation between initial amount of RA and residual stress were weak. Therefore, it is crucial to understand both the individual and coupled effects of residual stress and retained austenite on RCF life.

Research Objective

The objective of this study is to investigate the individual and coupled effects of retained austenite and compressive residual stresses on rolling contact fatigue through XFEM simulations. The results from simulations were then compared to experimental results. This study is mainly concentrate on crack propagation and rolling contact fatigue life due to the effect of austenite and compressive residual stress.

Research Approach

In modeling approach, finite element (FE) modeling was conducted to investigate the effect of austenite and residual on rolling contact fatigue of carburized steel. The finite element model was setup as shown in Figure 1. The FE model was based on the 'roller to ring contact' in the experimental Micro Pitting Rig (MPR) setup by PCS instrument (London, UK) [25], as shown in Figure 1a. The setup of a two-dimensional (2D) plane strain RCF model was created in commercial FE software, ABAQUS 6.14 as shown in Figure 1b. The dimension of the RCF model is 7*a* (height) by 10*a* (width), where '*a*' represents the half contact width of 100μm to match experimental conditions. The 2D quadrilateral, reduced element (CPE4R) was used in this model. A load corresponding to a maximum Hertzian pressure of 1.5 GPa was applied on the surface with repeated moving distance of 6*a*, in order to simulate the rolling contact between the ring and roller. The Hertzian load was defined by UTRACLOUD user-defined subroutine in ABAQUS. UTRACLOUD was created as a virtual surface load for the purpose of simplifying the simulations, so that the modeling of the ring and the contact interaction between the ring and roller can be eliminated. Voronoi Tessellation was implemented to simulate the nature effect of microstructure in the carburized steel. Different levels of retained austenite and residual stress

were incorporated in the model. eXtended Finite Element Method (XFEM) was used to simulate crack initiation and propagation in a two-dimensional finite element RCF model in ABAQUS.

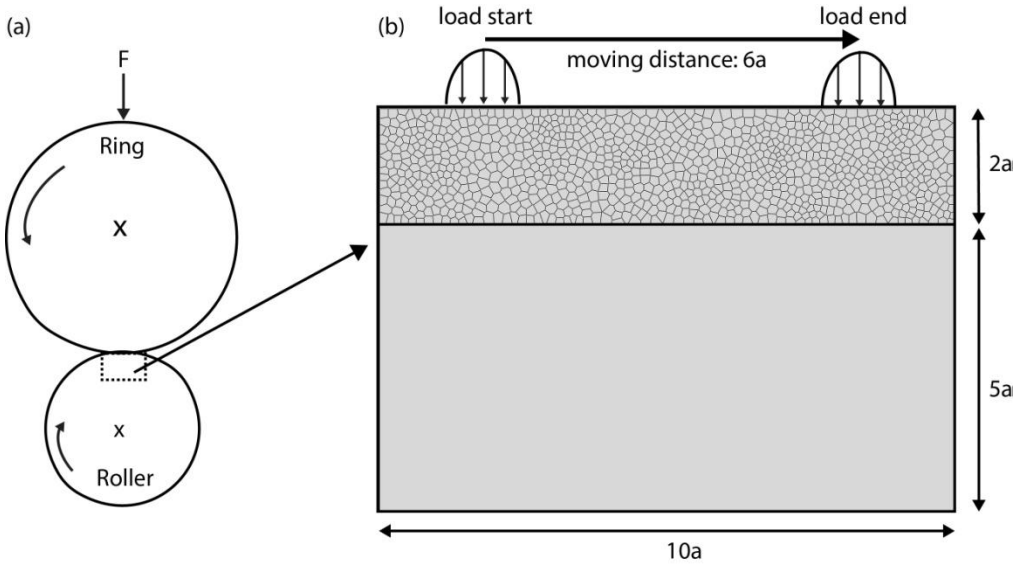

Figure 1. Finite element model setup: (a) Schematic diagram of a simplified rolling contact fatigue test from experiment; (b) a two-dimensional rolling contact fatigue model in ABAQUS

Thesis Organization

This thesis is organized into four chapters. The first chapter introduces the background, motivation and objectives of the research. The later part of the chapter overviews the research approaches in the study.

The second chapter conducts literature reviews related to the study, such as contact mechanics, Voronoi tessellations, and extended finite element method.

The third chapter consists of the manuscript submitted to the journal *Material Science and Engineering: A* titled: *Investigating the* e*ffect of retained austenite and residual stress on rolling contact fatigue of carburized steel with XFEM and experimental approaches*. The paper

was written by George Ooi and co-author Sougata Roy who contributed to the experimental work and analysis.

The fourth chapter concludes the findings from the study and provides recommendations for future works.

CHAPTER 2. LITERATURE REVIEW

Contact Mechanics

Contact mechanics is a subject that describes stresses and deformations which arise when the surfaces of solid bodies are in contact with each other. Contact mechanics was first originated by Heinrich Hertz when he presented that the contact surface between glass lenses was an elliptical area [26] in 1882. The well-known 'Hertzian' contact theory showed that the elastic displacements in the two bodies were compatible with the proposed elliptical area of contact. Several assumptions made in the Hertzian contact theory are that each body is considered as an elastic half-space; the contact surfaces are continuous and non-conforming; the material properties are linear elastic and isotropic; the contact between surfaces are frictionless. Figure 2 demonstrates the deformation of two non-conforming elastic bodies after a normal compressive load, *P*, was applied on both bodies 1 and 2 toward each other. The first contact point, *O*, was taken as the origin of a Cartesian coordinate system and was spread into an area after load, P, was applied. In the contact of solids of revolution or spheres, the contact area is circular. The contact surfaces touch at a point as a point contact. After a load, *P*, was applied, the arbitrary points T_1 and T_2 move toward the origins, which accumulates a total depth of indentation, δ, from the sum of indentations from each body δ_1 and δ_2 respectively. The relationship between the depth of indentation, δ, contact radius, a, and the body radius, R, is expressed as:

$$\delta = \frac{a^2}{R} \tag{2.1}$$

The contact radius is shown as:

$$a = \left(\frac{3PR}{4E^*}\right)^{1/3} \tag{2.2}$$

where E^* is the composite elastic modulus, as shown in the following equation:

$$\frac{1}{E^*} = \frac{1-v_1^2}{E_1} + \frac{1-v_2^2}{E_2} \tag{2.3}$$

E_1, E_2 and v_1, v_2 are the elastic moduli and Poisson's ratio respectively corresponding to body 1 and 2. Substitute equation (2.2) into (2.1), the total indentation becomes:

$$\delta = \left(\frac{9P^2}{16RE^{*2}}\right)^{1/3} \tag{2.4}$$

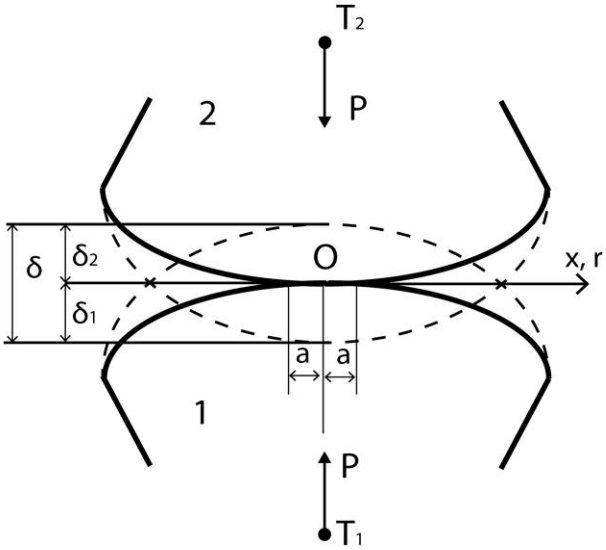

Figure 2. Hertzian contact between two non-conforming elastic bodies

The total load applied on the solids can be calculated by integrating the pressure applied over the contact area between two bodies, which is shown below:

$$P = \int_0^a p(r)(2\pi r)dr = \frac{2}{3}p_{max}\pi a^2 \tag{2.5}$$

Therefore, the maximum contact pressure, p_{max}, can be expressed as

$$p_{max} = \frac{3P}{2\pi a^2} \tag{2.6}$$

The contact area between two cylindrical bodies, whose long axes are parallel to the y-axis, is elliptical. Under zero loading, the contact surfaces between two cylindrical bodies touch along a line. According to Johnson [26], the half contact width, *a*, and the maximum contact pressure of two parallel cylindrical bodies are shown as:

$$a = \sqrt{\frac{4P\prime R}{\pi E^*}} \tag{2.7}$$

and

$$p_{max} = \frac{2P\prime}{\pi a} = (\frac{P\prime E^*}{\pi R})^{1/2} \tag{2.8}$$

where *P'* is the applied load per unit length. Detailed formulations and results for contact mechanics can be found in [26]. The pressure distribution which arises in this contact, proposed by Hertz is listed as:

$$p(x) = p_{max}\sqrt{1 - \left(\frac{x}{a}\right)^2}, \qquad x \leq a \tag{2.9}$$

where p_{max} is the maximum contact pressure applied on the roller by the ring, '*a*' is the half contact width.

In this study, the contact between the ring and roller is modeled according to the basis of contact mechanics under the investigation of rolling contact fatigue. Equation (2.9) is utilized as the load definition in the simulations. The Hertzian pressure produces a parabolic depression on the surface of an elastic body as shown in Figure 3. The range of contact pressure is in between $x = -a$ and $x = a$, where $p=0$ for both values. The body experiences localized maximum contact pressure when $x = 0$.

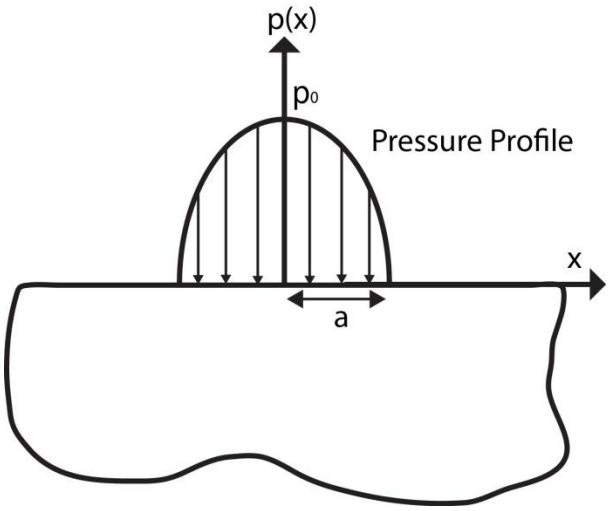

Figure 3. Hertzian contact: Parabolic pressure profile

Microstructure with Voronoi Tessellations

Voronoi Tessellation or sometimes refers to Voronoi diagram is a partition of the plane into regions with "*n*" convex polygons based on distance to points in a subset of the plane. Voronoi Tessellation has been used in many applications, such as in the fields of crystallography, computational geometry, metallography and etc. In this study, Voronoi diagram was used as computational geometry in order to divide an area of material into regions of grain microstructures. In a 2D problem, a set of finite points is given in the Euclidean plane. The number of finite points is assumed to be at least 2 or more ($2 \leq n < \infty$) but all points are unique that no points coincide in the plane. Those points are assigned randomly in the plane. According to the notations from [27], the n points are stated as p_1, p_2, …, and p_n and the corresponding coordinates are (x_{11},x_{12}), (x_{21},x_{22}), …,and (x_{n1},x_{n2}) or location vectors x_1, …, and x_n. Assuming p is an arbitrary point (x_1, x_2) in the plane or a location vector x, then the Euclidean distance between one of the '*n'* points and the arbitrary point will be:

$$d(p, p_i) = \|x - x_i\| = \sqrt{(x_1 - x_{i1})^2 + (x_2 - x_{i2})^2} \tag{2.10}$$

The arbitrary point, *p*, is assigned to every location in the plane. The closest arbitrary points, *p*, in the plane are assigned to the closest member p_i. If two or more members are equally close to the arbitrary point, then the arbitrary point is assigned to those members. Figure 4 showed that *p'* is an arbitrary point on the boundary between p_1 and p_3 since *p'* is equally close to them. The mathematical expression for the Voronoi diagram of each region can be expressed in the following way:

$$V(p_i) = \{x \mid \ \|x - x_i\| \leq \|x - x_j\| \, for \, j \neq i, \ and \ i, j \in I_n.\} \tag{2.11}$$

The regions are formed according to the set of locations assigned to the corresponding member in the point set as shown in Figure 4.

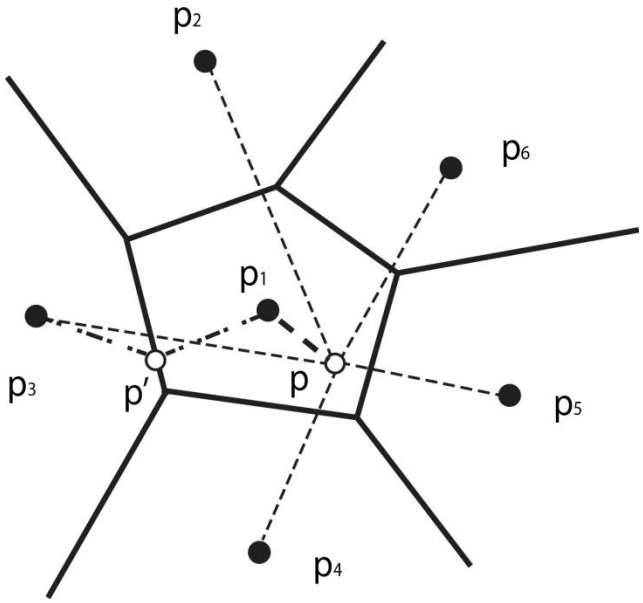

Figure 4. A planar ordinary Voronoi diagram

XFEM

Applying crack modeling techniques in FEM commercial software is extremely useful in predicting crack initiation and propagation without physically conducting experiments. Crack modeling techniques, such as XFEM, VCCT, and contour integral are readily available in the ABAQUS. In this study, the eXtended finite element method (XFEM) was chosen and implemented to model discontinuities such as cracks in ABAQUS. The reasons of using XFEM are because contour integral does not predict crack propagation, whereas VCCT only allows initiation and propagation of a crack along a pre-defined crack surface. Another constraint from both VCCT and contour integral are due the requirement of intensive meshes refinement near the crack tip in order to accurately capture the singular field. When modeling a moving crack with VCCT, the meshes are required to be updated constantly. These limitations are not suitable for modeling subsurface cracks which are not easily to be observed or predicted in experiments and to capture the randomness of microstructure effects.

Unlike conventional FEM, XFEM is an extension of conventional finite element that allows discontinuity to be presented in the elements, by implementing the special enriched functions with additional degrees of freedom coupled with the concept of partition of unity [28]. The approximation for a displacement vector function with the partition of unity enrichment consists of a standard finite element and the enrichments, which is shown in the equation below [28]:

$$u = \sum_{I=1}^{N} N_I(x)[u_I + H(x)a_I + \sum_{\propto=1}^{4} F_{\propto}(x)b_I^{\propto}] \quad (2.12)$$

The first term is the continuous part of FE, where $N_I(x)$ is the nodal shape function and u_I is the nodal displacement vector. The second term is for nodes whose shape function support is cut by the crack interior, where $H(x)$ is a discontinuous jump function across crack surfaces. The third term is applied to the nodes whose shape function support is cut by the crack tip [29], where $F_\alpha(x)$ is the elastic asymptotic crack-tip function and b_I^α is the nodal enriched degree of freedom vector. The cohesive segments method and phantom nodes were also applied in the model to simulate moving cracks [30, 31]. Since the crack propagation cuts through an entire element at a time in ABAQUS, equation (2.12) can be simplified into:

$$u = \sum_{I=1}^{N} N_I(x)[u_I + H(x)a_I] \tag{2.13}$$

The XFEM-based cohesive segment method was coupled with traction-separation law (TSL), which is defined by a damage initiation criterion and a damage evolution law for degradation of material stiffness. The materials lose their stiffness when the damage initiation criterion reaches 1 within a given tolerance and then followed by the linear damage evolution response [30]. The maximum normal stress criterion (MAXS) is used as the damage initiation criterion whereas the fracture energy dictates the degradation of material stiffness. MAXS for martensite and austenite were set as 225 and 460 MPa respectively with a critical crack length of 10 μm. The fracture energy can be calculated from the fracture mechanics equation:

$$Gc = K_c^2(1 - v^2)/E \tag{2.14}$$

where K_c is the fracture toughness, v is the Poisson's ratio and E is the elastic modulus. The fracture toughness of martensite and austenite were assumed to be 17.6 and 33 MPa-m½ respectively [32, 33]. Cracks were induced along the grain boundaries but cracks could

propagate along an arbitrary, solution dependent path depending on the weakest points in materials where damage initiation took place [30].

CHAPTER 3. INVESTIGATING THE EFFECT OF RETAINED AUSTENITE AND RESIDUAL STRESS ON ROLLING CONTACT FATIGUE OF CARBURIZED STEEL WITH XFEM AND EXPERIMENTAL APPROACH

Adapted from paper to be submitted to Material Science and Engineering: A

*George Theng Ching Ooi, Sougata Roy and Sriram Sundararajan**

Department of Mechanical Engineering, Iowa State University, Ames IA 50011, USA

srirams@iastate.edu

Abstract

In this study, the effects of retained austenite (RA) and residual stress on rolling contact fatigue (RCF) of carburized AISI 8620 steel were investigated through modeling and experiments. In modeling, a two-dimensional finite element RCF model was developed to examine the crack propagation and fatigue life of carburized AISI 8620 steel. An extended finite element method (XFEM) was used to initiate and propagate the cracks in the model. A Voronoi tessellation was randomly generated to simulate the randomness of the microstructures in steel. The cracks were initiated on the grain boundaries of a Voronoi cell prior to the simulations at different locations in the RCF model. The RCF life of the samples was determined by rolling contact fatigue tests. The results in both simulations and experiments showed that the higher level of RA and compressive residual stress achieved improved RCF life through mitigation of crack propagation. The effect of increased RA led to significant improvement on RCF life as compared to increased in compressive residual stress.

Introduction

Rolling contact fatigue (RCF) is a major cause of failure in rolling element bearings and gears, caused by cyclic loading of the material subjected to rolling or sliding contact. The common failure modes are due to surface or subsurface initiated cracks which eventually propagate and lead to pitting or spalling. Surface cracks can be initiated due to improper surface finishing, improper use of lubricant or flaws on surfaces. Modern bearing steels and gears are clean and well lubricated and therefore subsurface cracks are more likely to be initiated due to the effect of the maximum normal stress or alternating shear stress under rolling contact below the surface [2, 3].

Over the decades, researchers and engineers have been working on improving the RCF life and reliability of the rolling element bearings and gears. Operations such as heat treatments are performed to improve the fatigue life by inducing residual stress and retained austenite in the materials [10, 12, 34, 35]. It is well known that compressive residual stress improves fatigue life [9, 13-15, 36]. Retained austenite (RA) is austenite that does not transform to martensite upon quenching. Several studies have investigated the effect of RA in the fatigue behavior and stability of steel [16, 18-21, 36-38] and reported conflicting results. Da Silva's studies [21] found that higher levels of RA in carburized case of AISI 8620 steel prolonged fatigue life. Hu et al. [16] proposed an energy criterion method that showed austenite would decrease fatigue life when the propagation of the fatigue crack tip was more than the energy due to phrase transformation from austenite to martensite.

While the literature typically accounts for the individual effect of retained austenite or residual stress, the coupled effects of retained austenite and residual stress are extremely

important [9, 15, 16, 18-21]. The amount of residual stress induced in the material may depend on the amount of retained austenite [8, 22]. According to [23], increasing the level of retained austenite could decrease the amount of residual stress in steel due to lesser transformation from austenite to martensite upon quenching which accompanied with the volume expansion that induced the compressive residual stress. However, in previously reported experimental studies [10, 24], the correlation between initial amount of RA and residual stress were weak. Therefore, it is crucial to understand both the individual and coupled effects of residual stress and retained austenite on RCF life.

The purpose of this study is to investigate the effect of retained austenite and residual stresses individually and mutually on rolling contact fatigue of AISI 8620 steel through finite element method based simulations. The study was primarily focused on crack propagation and the RCF life. The results of the simulations were compared to the experimental results on AISI 8620 steel samples with different amounts of retained austenite and residual stress. The correlations between the retained austenite, residual stresses, and fatigue life are discussed for both simulations and experiments.

Modeling Approach

Finite Element Model

The finite element model used in this study was created to investigate the effect of retained austenite and residual stresses on RCF and to closely simulate cylinder on cylinder contact conditions used in experiments. The contact condition is shown in Figure 5 and is best described as follows: a load, F, was applied on a ring, with radius of R_1, which exerted a non-

conforming contact with a roller, with radius of R_2. Figure 5 illustrates how the model was simplified from a 3-dimensional (3D) problem, shown in Figure 5(a), to 2D, shown in Figure 5(b) and to a roller with moving contact load that simulated the rolling contact between the ring and roller as shown in Figure 5(c).

The size of the Hertzian contact characterized by the contact half-width, a, was chosen to be 100 μm to approximate experiments. A 2D plane strain RCF model was developed in ABAQUS 6.14. The RCF model was the primary focus within the representative volume element (RVE), which was the region where RCF stresses were found to be largest. Accordingly, the model was set up as a rectangle of width 10a and height 7a, where a=100μm. The schematic of the model setup in ABAQUS is shown in Figure 6. The RVE was enclosed from the top surface, y=0 to a depth of y=2a and the left surface x=-5a to the right surface x=5a. The RVE was divided into 1000 Voronoi cells to simulate the microstructure, where each cell has an average grain size of around 15 μm [39]. The entire domain was applied using quadrilateral, reduced elements (CPE4R). A moving load was applied on the surface from -3a to 3a to simulate the rolling contact between ring and roller. Initial subsurface cracks were initiated within this region with XFEM. The fatigue life of rollers was determined by the number of contact cycles that occurred for the cracks to propagate from the initial location to the surface.

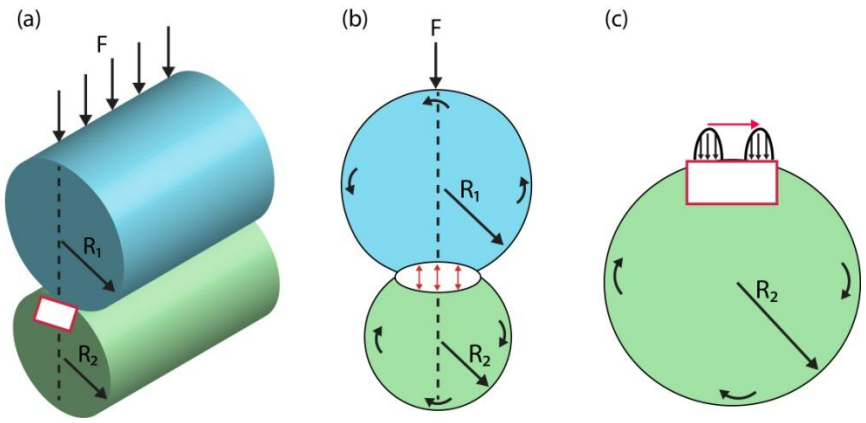

Figure 5. (a) 3D RCF model: ring, R_1, and roller,R_2 ; (b) 2D RCF model; (c) Simplified 2D RCF model: a roller with moving contact load that represents the rolling contact between ring and roller.

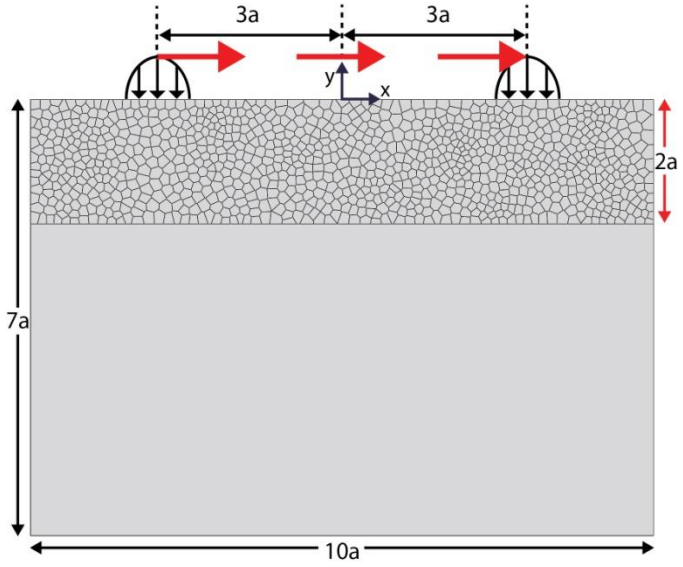

Figure 6. The schematic of ABAQUS RCF model showing the representative volume element; 'a' is the Hertzian contact semi-width from experiments.

Modeling Microstructure with Voronoi Tessellations

In this study, Voronoi Tesselation [27, 40-42] was used to model the random nature of the steel microstructure. Voronoi Tessellation is a partitioning of a plane into regions with a number of convex polygons. A random finite number of unique seed points, n, are assigned on a

plane to form ‘n’ regions. Each region is divided based on the closest Euclidean distance between points in a subset of the plane and one of the seed points, p_i, where $1 \leq i \leq n$. If the points in a subset of a plane are equally close to two or more seed points, then those subset points are assigned to the corresponding seed points and formed as the boundary points that divided those regions. Detailed mathematical formulations and applications of Voronoi Tessellation can be found in [27].

The microstructure distribution was expected to be varied in each sample even if the samples were produced from the same batch in experiments. Therefore, in this study, Voronoi Tessellation was generated in the RVE during simulations, in order to better capture the randomness effect of microstructure distribution in steel. Every simulation was generated with a new and randomized Voronoi diagram and microstructure distributions. Retained austenite and martensite were randomly distributed among the 1000 Voronoi cells, as shown in Figure 7. Each Voronoi cell represents an individual microstructure material with different shapes and orientations. The Voronoi cells and the distribution of microstructures were generated by a MATLAB script, the flowchart for which is shown in Figure 8.

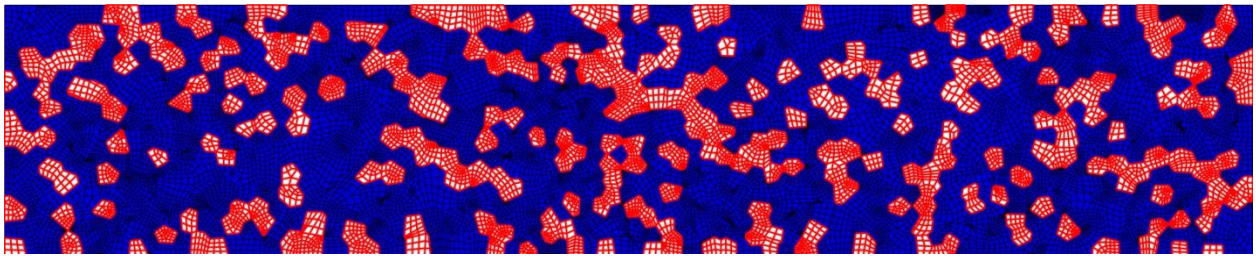

Figure 7. A 1000 Voronoi Tessellations with RA ~70% (blue) and Martensite (red).

Load and Boundary Conditions

As described previously, a moving load was applied on the top surface of the RCF model from, as shown in Figure 6. In this study, one cycle corresponds to the load moving across the surface from x = -3a to x = +3a. The moving load was determined by a user-defined subroutine, UTRACLOUD. UTRACLOUD was written for the purpose of simplifying the simulations and saving computational expenses and time. The subroutine acts as a virtual surface load in the form of Hertzian contact pressure applied on the roller by the ring, without actually modeling the ring and the contact interaction between the ring and roller. Test simulations for the subroutine were performed using the RCF model as shown in Figure 6, but without any Voronoi cells and microstructures. The results were compared to the Hertzian pressure equation [26],

$$p(x) = p_{max}\sqrt{1 - \left(\frac{x}{a}\right)^2}, \qquad x \le a \tag{3.1}$$

where p_{max} is the maximum contact pressure applied on the roller by the ring, and a is the half contact width.

Figure 9 shows that the user-defined UTRACLOUD subroutine was comparable with the Hertzian pressure equation, thus providing confidence in its use.

The boundary conditions of the left and right surfaces at y= -5a and y=5a were fixed at the displacement in x-direction and the bottom surface at x=10a was fixed at the displacement in y-direction. To incorporate residual stress in the model, an initial stress condition was defined from the top surface down to a depth of y=20 ± 10 μm, as shown in Figure 10. This is the reference zone where the residual stress is typically measured by XRD in experiments [43].

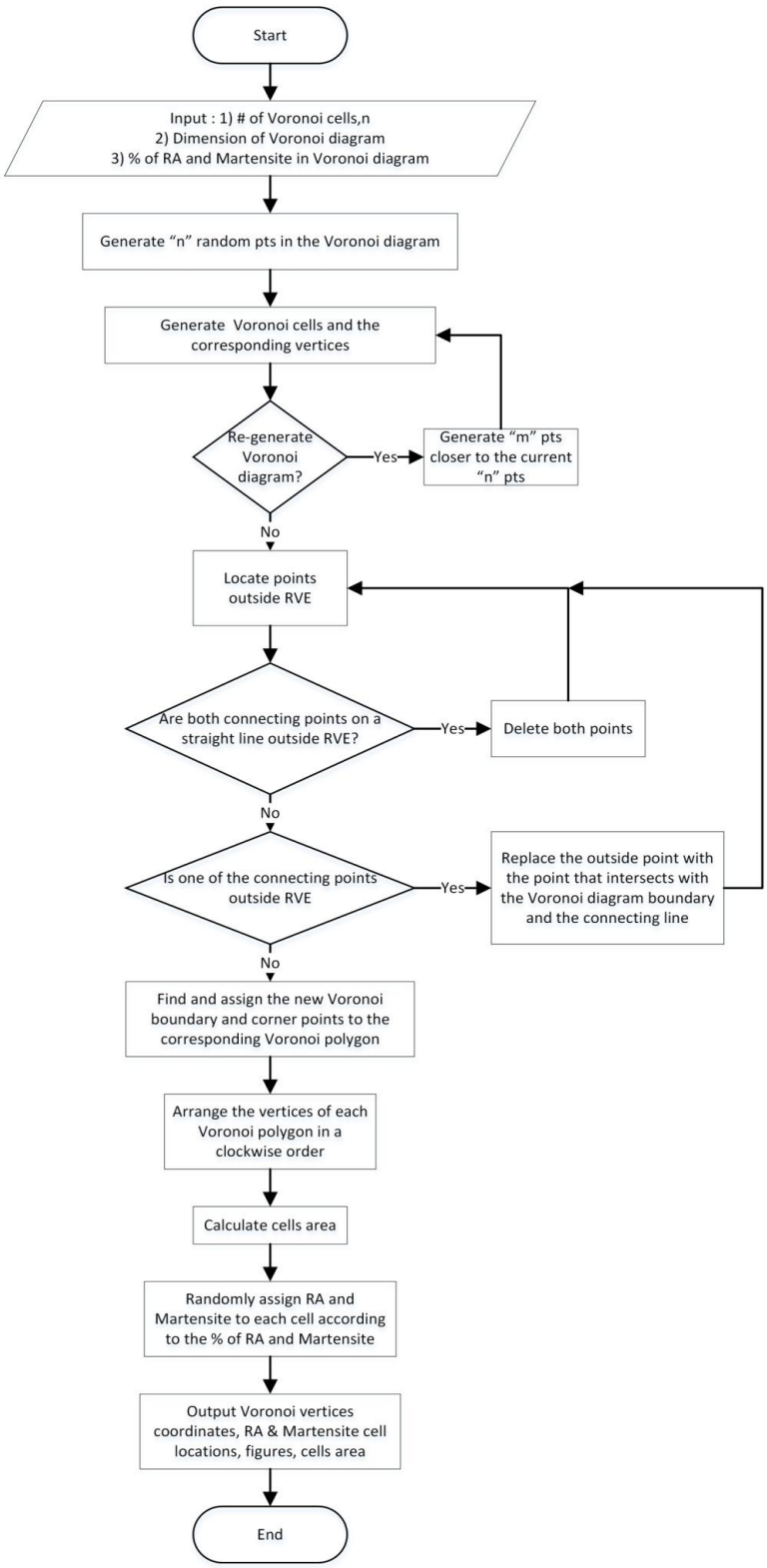

Figure 8. Flowchart for MATLAB script to generate Voronoi cells and microstructure distribution.

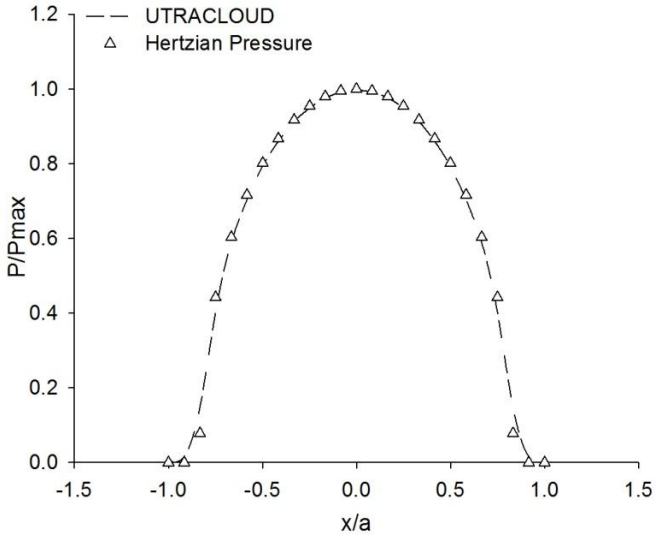

Figure 9. Hertzian contact pressure profile comparison between analytical values and simulation.

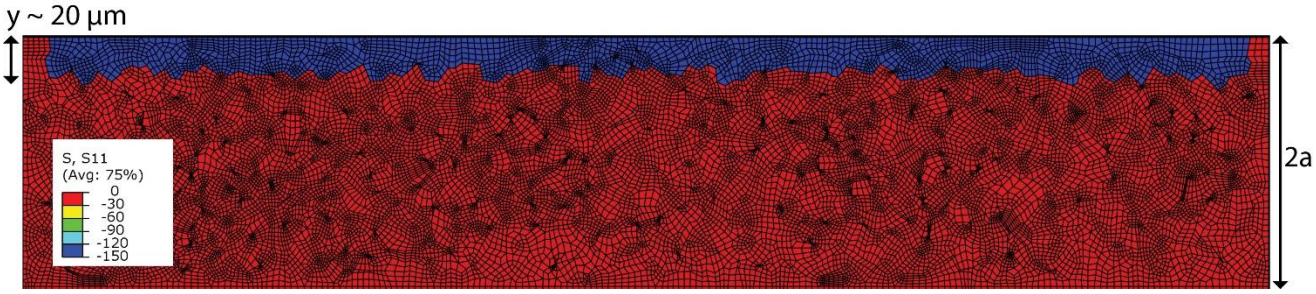

Figure 10. Schematic indicating regions experiencing residual stress. Here a 150 MPa compressive residual stress (blue) was applied on the top surface of the model.

Modeling Cracks with XFEM

The eXtended Finite Element method (XFEM) is a numerical method that is specially designed for discontinuities such as cracks. XFEM allows the presence of discontinuity by applying special enriched functions with additional degrees of freedom through the partition of unity concept [28]. Compared to conventional FEM, the advantages of implementing the XFEM

technique are that predefined propagation direction for cracks and intensive meshes around the cracks are not required [30]. The approximation for a displacement vector function *u* with the partition of unity enrichment consists of a standard finite element and the enrichments. The approximation is defined as [28]:

$$u = \sum_{I=1}^{N} N_I(x)[u_I + H(x)a_I + \sum_{\propto=1}^{4} F_{\propto}(x)b_I^{\propto}] \quad (3.2)$$

The first term consists of the continuous part of FE, which is the nodal shape function, $N_I(x)$ and nodal displacement vector, u_I. The second term is applied to nodes whose shape function support is cut by the crack interior. This term, $H(x)$, a discontinuous jump function across crack surfaces, is defined as [44]:

$$H(x) = \begin{cases} 1 & \text{if } (x - x^*) \cdot n \geq 0 \\ -1 & \text{otherwise,} \end{cases}, \quad (3.3)$$

where x is the sample Gauss point, x^* is the point on the crack closest to x and n is the unit outward normal to the crack at x^* and a_I is the nodal enriched degree of freedom vector. The last term is applicable to nodes whose shape function support is cut by the crack tip [29]. $F_{\alpha}(x)$ is the elastic asymptotic crack-tip function:

$$F_{\propto}(x) = \left[\sqrt{r}\sin\frac{\theta}{2}, \sqrt{r}\cos\frac{\theta}{2}, \sqrt{r}\sin\theta\ \sin\frac{\theta}{2}, \sqrt{r}\sin\theta\ \cos\frac{\theta}{2}\right], \quad (3.4)$$

where (r,θ) is a polar coordinate system with its origin at the crack tip. Hence, $\theta = 0$ is tangent to the crack at the tip and b_I^{α} is the nodal enriched degree of freedom vector. Figure 11 illustrates the coordinates for the discontinuous jump function and crack tip function on a smooth crack.

The moving cracks were modeled with the cohesive segments method coupled with phantom nodes [30, 31]. In XFEM-based cohesive segments method, the crack can initiate and

propagate along an arbitrary, solution dependent path in the bulk materials, because the crack propagation is not attached to the element boundaries in a mesh. Therefore, the near-tip asymptotic singularity is not required as the problem is simplified such that the crack propagates across an entire element at a time. In this case, equation (2) can be simplified into:

$$u = \sum_{I=1}^{N} N_I(x)[u_I + H(x)a_I] \quad (3.5)$$

To represent the discontinuity of cracked elements, phantom nodes were implemented. Phantom nodes are nodes that superpose on the original real nodes. They are fixed at the position of the corresponding real nodes when the element is intact. But when a crack cuts through an element, the phantom nodes separate from the corresponding real nodes. The element splits into two parts, with each part consisting of some real nodes and phantom nodes, depending on the crack orientation.

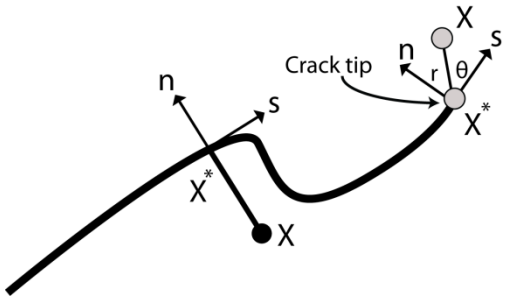

Figure 11: Normal and tangential coordinates for a smooth crack.

A traction-separation law (TSL) is implemented in XFEM along with the cohesive segments method. The TSL is defined by a damage initiation criterion and a damage evolution law for degradation of material stiffness. A crack is initiated or an existing crack propagates when the damage initiation criterion reaches the value of 1 within a given tolerance [30]. Once the damage initiation criterion is met, the materials are assumed to lose their stiffness followed

by a linear damage evolution response. The damage initiation and damage evolution are determined by the maximum normal stress criterion (MAXS) and fracture energy respectively in this study. Figure 12 shows a linear traction-separation response with a failure mechanism. The material properties for austenite and martensite are listed in Table 1.

Crack propagation is the main focus of this study. Therefore, a subsurface crack was incorporated into the microstructure prior to the simulation. The cracks were induced along the grain boundaries in between the grain cells and were allowed to propagate along or through the grain boundaries during the simulations. A new crack was created in each simulation at each RA% and residual stress at 9 different crack locations (combination of 3 different x locations and 3 different y locations), as shown in Figure 13. Figure 13 also shows an example of a crack at location #3 (x=2.5a, y=0.75a) in the RCF model. All cracks were randomly selected to the nearest defined coordinates with an average initial crack length of 10μm.

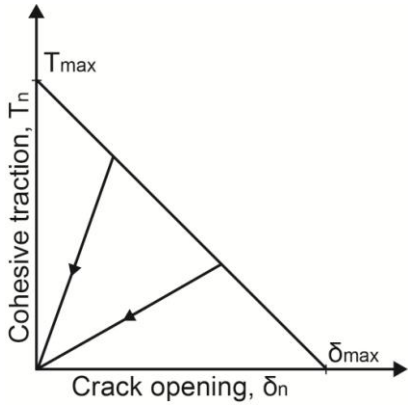

Figure 12. Linear damage evolution response of traction separation in XFEM. Damage initiation begins when $T_n = T_{max}$, the maximum cohesive traction, and followed by linear degradation behavior until δ_n reaches δ_{max}, the maximum crack opening.

Table 1. Material properties

	Symbol	Martensite	Austenite	Units
Elastic modulus	E	228[a]	200[c]	GPa
Poisson's ratio	v	0.3[a]	0.3[c]	-
Critical Fracture toughness	K_c	17.6[b]	33[d]	MPa-m½
Critical Fracture energy[e]	G_c	1.2	4.9	N/mm
Critical stress[f]	σ_c	3	6	GPa
MAXS[g]	σ_{maxs}	225	460	MPa
Avg. critical crack length	a_c	10		µm

[a] [45]; [b] [32]; [c] [46]; [d] [33]; [e] Calculated from $G_c=K_c^2(1-v^2)/E$;
[f] Calculated from $\sigma_c= K_c/(\pi a_c)^{1/2}$;
[g] Calculated from MAXS = σ_c/13; where 13 is a ratio factor in order to accelerate the simulations

Crack #	x/a	y/a
1	2.5	0.25
2		0.50
3		0.75
4	0	0.25
5		0.50
6		0.75
7	-2.5	0.25
8		0.50
9		0.75

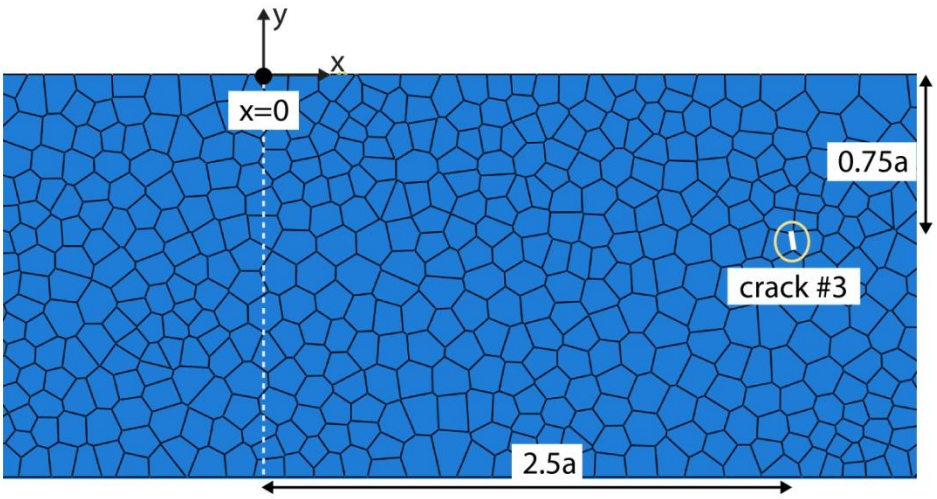

Figure 13. Cracks were placed individually at 9 different locations in the simulations as listed. Also shown is an example of a crack placed at location #3 (x=2.5a, y=0.75a) in the RCF model.

Experimental Approach

Sample Preparation and Characterization

In this study, samples with different levels of RA and residual stress were achieved by carburizing and tempering [10, 24, 47]. Increasing carbon potential suppresses martensite start (M_s) and martensite finish (M_f) temperature [24]. This results in incomplete conversion of austenite to martensite and helps to increase retained austenite content on surface. On the other hand, increasing tempering temperature and time help to convert existing retained austenite to martensite [47]. In this study, the carbon potential was varied from 1.2 to 2%. The tempering temperature and time were varied from 50°C for 1 hour to 400°C for 2 hours. Table 2 lists the percentage of RA and the amount of compressive residual stresses of the samples after heat treatment. A Rigaku SmartLab X-ray diffractometer with micro-diffraction capability was used to quantify RA percentage of the samples after heat treatment. A Cu Kα target (wavelength 1.54 Å) was used with a target voltage of 40 KV and current 44 mA. XRD scan data for a range of 40 to 93 degrees (2θ angle) was analyzed using TOPAS software to determine the amount of RA in those samples. TOPAS uses the Rietveld method which helps to fit theoretical data to a measured pattern using analytical profile functions & least square methods [12, 48-50].

Table 2. Retained austenite and compressive residual stress levels on the carburized samples.

RA level	**RA [%]**	**Residual stress [MPa]**
Low RA	0.4±0.2	479.6±15.6
Medium RA	14.5±1.9	268±42.4
High RA	69.7±3.7	155.4±41.9

The residual stress levels of the samples were measured using Cr XRD (wavelength 2.29 Å) with a target voltage of 35KV and current of 1.5 mA. For these measurements, the (211)-peak of Cr Kα radiation was used to determine the peak positions that were used for residual stress determination. Carburizing helped to generate compressive residual stress on all sample surfaces. High temperature tempering resulted phase transformation of austenite to martensite. This helps in expansion of surface layer due to volumetric expansion during phase transformation [47]. Consequently, higher compressive residual stresses were observed in lower RA samples. RA and residual stress on the samples prepared by three different heat treatment schemes are mentioned in Table 2. For further discussion, these three levels of RA are approximately mentioned as 70%, 15% and 0% RA as high, medium and low levels of RA. The samples were ground and polished to achieve average surface roughness level 0.19-0.24 μm over a scan size of 1 mm × 0.6 mm prior to experiments.

Rolling Contact Fatigue Tests

Rolling contact fatigue tests were performed using a Micro Pitting Rig (MPR) by PCS instruments (London, UK) [25]. A schematic representation of the experimental setup is shown in Figure 14. The MPR is a computer controlled disc-on-disc contact instrument in which a central roller (sample) is in contact with three harder counter face rings as shown in Figure 10. The roller therefore experiences three contact cycles per revolution at a constant contact pressure. The speeds of the rings and rollers are controlled independently which allows different combinations of rolling and sliding contact. The MPR utilizes a dip lubrication system, with the oil level 27.8 millimeters below the center of the roller and a sump volume of 150 milliliters. The unit is also temperature controlled to maintain the desired operating temperature of lubricant

sump. A chamfered roller with face-width 1mm was used for the tests performed in this study. The diameter for roller was 12 mm and for rings 54.15 mm.

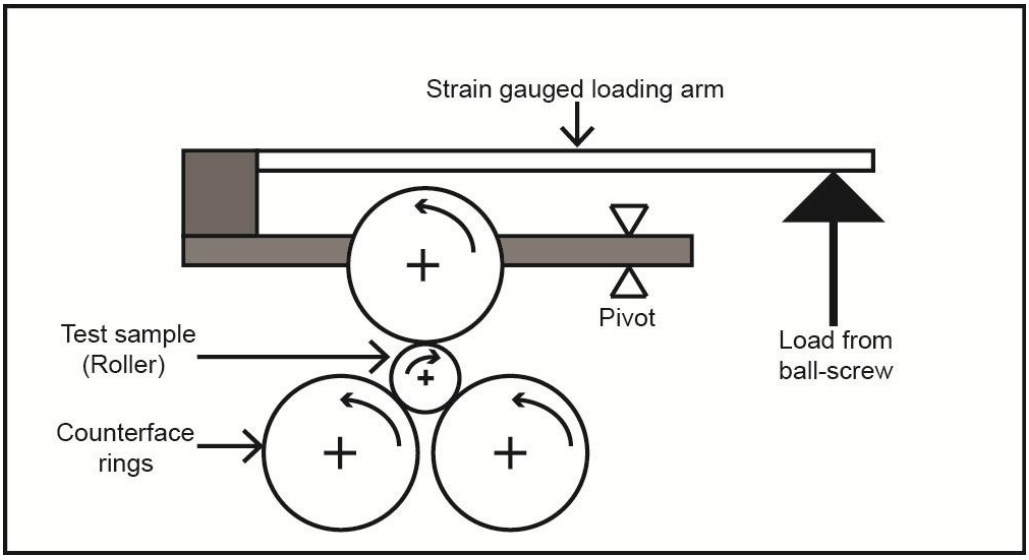

Figure 14. Schematic diagram of rolling contact fatigue test rig.

All tests were conducted using the conditions listed in Table 3. Tests were conducted with maximum Hertzian contact pressure level of 1.5 GPa. The normal load resulted is listed in `Table 3. The relative amount of rolling and sliding is determined by the slide-to-roll ratio (SRR) and is defined as follows:

$$\text{SRR}\ (\%) = \frac{U_1 - U_2}{1/2(U_1 + U_2)} \cdot 100 \qquad (3.6)$$

where U_1 is the speed of the roller and U_2 is the speed of the rings. An accelerometer attached to the instrument provides peak to peak (P/P) and centre-line-average (CLA) values of vibration due to crack propagation and surface deformation during RCF tests. All experiments were run up to 50 million contact cycles or till the system detected a P/P accelerometer signal of 10g, whichever occurred first. Each experiment was associated with a 2 minutes time duration ‘ramp-

up' step where the test parameters were ramped to pre-set conditions (as mentioned in `Table 3) for the upcoming fatigue step.

The lubricating oil used in this study an API group II base oil with ZDDP anti-wear and other additives, one of which was a viscosity index (VI) improver. Hence the lubricating oil was sheared before testing by running it through piston pump for 48 hours to ensure no change in viscosity occurred due to shearing during rolling contact fatigue tests. The kinematic viscosity of the sheared oil was 50.51–51.44 cSt at 40 °C and 7.56–7.81 cSt at 100 °C.

`Table 3. Operating test conditions.

Test parameter	
Entrainment velocity (m/sec)	1.75
Slide to roll ratio (%)	20
Normal Load (N)	311
Maximum contact pressure (GPa)	1.5
Lubricant sump temperature (°C)	80
Oil film thickness (nm)[a]	80
Lambda ratio	0.16

[a]: Estimated using Eq. (3.7)

Minimum oil film thickness (H_{min}) for the experiments was calculated using the Hamrock-Dowson's equation mentioned below,

$$H_{min} = 1.714U^{0.694}G^{0.568}W^{-0.128} \quad (3.7)$$

where U is dimensionless speed parameter, G is the dimensionless material parameter, and W is the dimensionless load parameter. The film thickness ratio (λ) was calculated using H_{min} and measured by initial composite roughness (Rq). All tests were run on boundary lubrication.

Results and Discussion

Simulations Results

The XFEM RCF model was used to investigate the crack propogation rate and fatigue life of AISI 8620 steel with different amount of RA and residual stress. Figure 15 shows the average number of contact cycles that took cracks from initial location to the surface at different RA percentages and residual stresses. The results were obtained by nine randomly generated Voronoi Tesselations for each case in order to ensure statiscally valid results. The results indicate that the number of contact cycles for the cracks to reach the surface increases as the RA increases from 0 to 70% when the amount of residual stress remains constant. The results are consistent with experiments that have reported that the fatigue life improves as the amount of RA increases [21]. Figure 15 also illustrates that the compressive residual stress prolongs the number of cycle for the cracks to reach the surface when residual stress increases from 0 to 500 MPa when the amount of RA is unchanged. This beneficial effect of compressive residual stress on fatigue life is well understood [9, 13-15, 36].

Figure 16 shows the results of the average crack growth rate for different RA percentages and residual stress. The results showed that the higher the percentage of RA, the slower the average crack growth rate, irrespective of the level of compressive residual stress. Similarly, the average crack growth rate decreases when the residual stress increases at 0, 20 and 70% RA. From these results, it is clear that increasing retained austenite and residual stress inhibits the fatigue crack growth, consistant with previous studies [51, 52].

Table 4 and Table 5 summarize the results of the beneficial impact of RA and compressive residual stress on the rolling contact fatigue life. The rolling contact fatigue life implies the number of cycle for the cracks to reach the surface. The results from Table 4 compares to the RCF life without residual stress at the same percentage of RA as the baseline. For example, the RCF life extended by 180% at 0% RA with 500 MPa compressive residual stress as compared to 0% RA without residual stress. By comparison, the RCF life increases by 36% at 70% RA with 500 MPa residual stress as compared to its baseline. Therefore, the results show that the effect of residual stress is more prominent when the material consists of a little amount of RA to none.

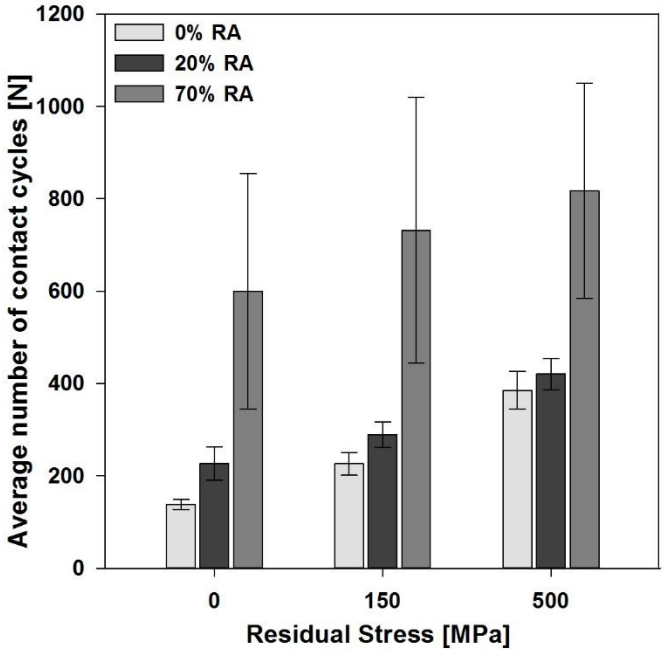

Figure 15. The average number of contact cycles for crack reaching the surface from initial locations at various RA% and compressive residual stress in simulations. Error bars represent 90% confidence intervals.

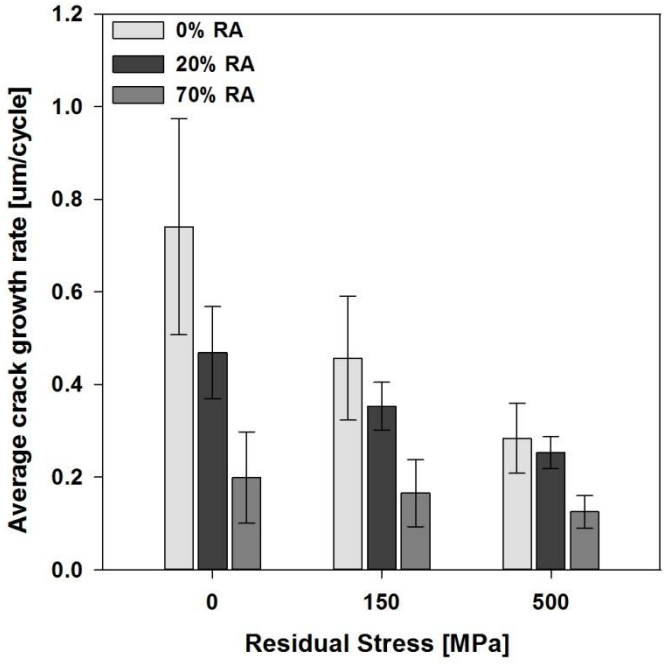

Figure 16. The average crack growth rate at various RA% and compressive residual stress in simulations. Error bars represent 90% confidence intervals.

On the other hand, Table 5 compares the results to demonstrate the effect of RA as compared to the 0% RA case with the same amount of residual stress as the baseline. In this case, 70% RA without residual stress extended the RCF life about 337% as compared to the case of 0% RA without residual stress. However, there was only 9% increased in RCF life at 20% RA with 500 MPa residual stress as compared to its baseline. The results indicate that high RA (70%) with low residual stress (0 MPa) are preferable than low RA (0%) with high residual stress (500 MPa) in term of RCF life. Similar trends were also observed in Shen's [36] simulation results, where he showed that the L_{50} life for carburized AISI 8620 steel with high RA (~35%) and low compressive residual stress (0.15 GPa) had about 10 times larger than the case with low RA (0%) and high compressive residual stress (0.8 GPa). The results of the model

therefore suggest that a high level of RA is beneficial to RCF and that RA content has a more significant impact on RCF life than residual stress.

Table 4. Effect of residual stress on the relative RCF life improvement comparing to baseline (without residual stress).

Retained austenite [%]	**Residual stress [MPa]**	**[a]Relative RCF life improvement [%]**
0	150 500	64.1% 180%
20	150 500	28.1% 85.9%
70	150 500	22.1% 36.0%
[a]Relative RCF life improvement = ([1]change - [2]baseline)/baseline [1]change = average RCF life with residual stress (and same RA % with baseline) [2]baseline = average RCF life without residual stress		

Table 5. Effect of RA on the relative RCF life improvement comparing to baseline (0% RA).

Retained austenite [%]	**Residual stress [MPa]**	**[a]Relative RCF life improvement [%]**
20	0 150 500	64.1% 28.1% 9.06%
70	0 150 500	337% 224% 111%
[a]Relative RCF life improvement = ([1]change - [2]baseline)/baseline [1]change = average RCF life with RA (and same residual stress with baseline) [2]baseline = average RCF life without RA (0%)		

Experimental Results

Table 6 shows the rolling contact fatigue lives of samples with different level of retained austenite and residual stress obtained from the experiments. The results show that higher RA helped improve RCF life of carburized samples significantly, up to 12 times from 0% to 70% RA. This observation is consistent with the predictions from the simulations.

Table 6. Rolling contact fatigue life (P/P accelerometer to reach 10g)

Sample		**RCF life**
70% RA	Test 01	> 50 million
	Test 02	> 50 million
15% RA	Test 01	15 million
	Test 02	17.5 million
0% RA	Test 01	4 million
	Test 02	2.5 million

Comparative Study between Computation and Experimental Observations

The following simulations were then performed to closely match the RA and residual stress of the experimental test samples: case 1 with 0% RA and 500 MPa compressive residual stress; case 2 with 15% RA and 285 MPa compressive residual stress; and case 3 with 70% RA and 155 MPa compressive residual stress.

Figure 17 indicates the ratio of RCF life compared to case 1 which was obtained from simulations and experiments. Both results show an increasing trend in RCF life from case 1 to case 3, when the amount of RA increases from 0% to 70% though the compressive residual stress decreases from 500 to 155 MPa. This result is aligned with the Shen's results [36], where the fatigue life of carburized AISI 8620 steel was mostly dependent on the amount of RA in the

samples. Though the compressive residual stress improves the fatigue life as well, it is less effective than RA in doing so.

Some discrepancies in the magnitude of the ratio of cycle life are expected between modeling and experimental results from case 1 to 3 as seen in Figure 17, since in experiments the effect of RA and residual stress have significant roles in improving the RCF life during the crack initiation process as well as crack propagation to failure. In the simulations, a crack was initiated at the beginning of the simulation whereas there is no such guaranteed pre-existing condition in the experiments. In addition, the RCF life in the simulation does not account for plastic deformation that can occur during the experiments. Consequently, it is reasonable to expect the simulations to underestimate the RCF life compared to the experiments. However, the model does indicate that crack propagation is significantly hindered due to presence of RA, thus showing increasing RCF life with increasing RA, consistent with experiments.

An ABAQUS output of the corresponding scalar stiffness degradation (SDEG) of a modeling result are shown in Figure 18. SDEG represents the damage condition on the material's stiffness with a scale from 0 to 1, where 0 is undamaged and 1 is completely damaged. When SDEG reaches 1, the corresponding elements are removed from the meshes, which represent the crack opening. In experiments, the 15% RA sample failed very quickly due to early crack initiation and rapid crack propagation. During fatigue loading, stress induced phase transformation of retained austenite to martensite takes place ahead of cracks which hinders propagation of crack. Higher retained austenite creates more barriers to crack propagation which results higher rolling contact fatigue life. Similarly, it was observed in simulations that a crack propagated toward the easiest path which is usually the neighboring martensite grains as those

exhibit lower fracture energy than austensite. If a crack was surrounded by austenite, which is most likely in the 70% RA sample, the propagation of cracks was temporarily hindered. At this point, the crack would not continue to grow to the next grain until the localized stress induced by the rolling contact overcomes the damage initiation criterion and is followed by the deterioration of grain's stiffness till failure.

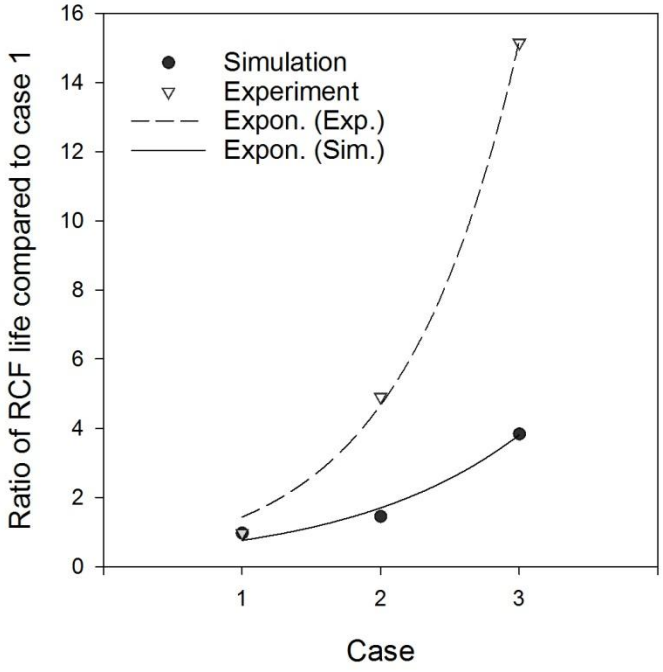

Figure 17. Ratio of RCF life compared to case 1 from simulations and experiments. Case 1: 0% RA with 500 MPa compressive residual stress; Case 2: 15% RA with 285 compressive residual stress; and Case 3: 70% RA with 500 compressive residual stress.

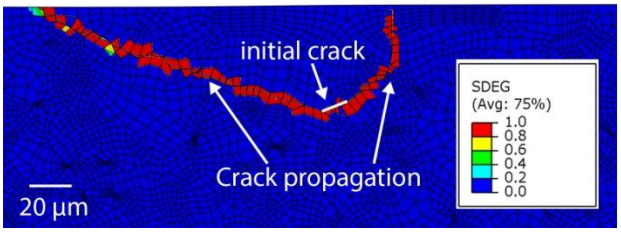

Figure 18. An ABAQUS output of the scalar stiffness degradation, SDEG.

Conclusions

This paper investigates the effect of retained austenite and residual stress on the rolling contact fatigue behavior of carburized AISI 8620 steel both numerically and experimentally. A 2D RCF XFEM model was created to observe and compare the RCF life with a range of retained austenite from 0% to 70% and compressive residual stress from 0 MPa to 500 MPa. The simulation results showed that higher levels of retained austenite and residual stress in carburized AISI 8620 steel improves the cycle life of rolling contact fatigue and decreases the average crack propagation rate. These were consistent with the experimental results, which showed that the 70% RA with 155 MPa compressive residual stresses sample had much higher cycle life than the 15% RA with 285 MPa compressive residual stress and 0% RA with 500 MPa compressive residual stress samples.

Both experimental and modeling results show that the effect of retained austenite is much more significant than the effect of residual stress on the RCF life of carburized AISI 8620 steel. The study suggests that a high level of RA with low compressive residual stress is preferable than low level of RA with high compressive residual stress to enhance the rolling contact fatigue life of carburized steel.

CHAPTER 4. CONCLUSION AND FUTURE RESEARCH

Specific Findings

The effect of retained austenite and residual stress on the rolling contact fatigue behavior of carburized steel through simulations and experiments were investigated in this study. The two-dimensional RCF XFEM simulations were conducted based on the amount of retained austenite and residual stress measured in experimental studies. Three cases were performed in simulations, which are 0% RA with 500 MPa compressive residual stress, 15% RA with 285 MPa compressive residual stress and 70% RA with 155 MPa compressive residual stress. The simulation results indicates that higher levels of retained austenite and residual stress in carburized steel improves the cycle life of rolling contact fatigue and hinders the average crack propagation rate. The simulations results were aligned with the experimental results which show that the rolling contact fatigue cycle life of 70% RA with 155 MPa compressive residual stress samples were much higher than the 15% RA with 285 MPa RS and 0% RA with 500 MPa samples. The study suggests that a high level of RA with low compressive residual stress is preferable than low level of RA with high compressive residual stress to enhance the rolling contact fatigue life of carburized steel. Overall, both results from experiments and simulations demonstrate that the higher amount of retained austenite and residual stress improve the rolling contact fatigue life of carburized steel.

Future Work and Recommendations

In the present study, the amount of RA and RS used in the simulation was based on the initial measured RA and RS from the experiments. Those values remained constant throughout the simulations. The author suggests that the models could be improved by mimicking the evolution of RA and RS according to the experimental data because the amount of RA and RS varied throughout the experiments. This will accurately capture the effect of RA and RS from beginning to the end of cycle.

In order to maximize the efficiency, a subsurface crack was initiated in the beginning of the simulations. The current XFEM models disregard the facts that happened before the crack initiation and only take the rolling contact cycles from crack initiation to propagation and to material failure into consideration. Another recommendation would be running the simulations before the crack was initiated and applying a customized crack initiation subroutine that matches the experimental observations.

In the current model, the Hertzian moving load was not applied on -5a to -3a and 3a to 5a. Periodic boundary conditions can be included in the model so that an infinite Hertzian load condition is repeatedly moving throughout the top surface of the Voronoi regions without leaving area that was not applied by the load condition. When the load comes to an end of the Voronoi region, the other load will enter through the opposite end with exactly the same Hertzian load condition and direction. This method can represent the load conditions in the rolling contact in a more realistic manner.

Another future work may be including a 3D XFEM Voronoi Tessellations model coupled with the plasticity theory. Although 3D model is more computational expensive than 2D model, it allows cracks to grow in the out-of-plane direction which results in more accurate analysis. Besides, XFEM coupled with large plastic deformation may unveil more realistic material behaviors and microstructure that are similar to the experimental results.

REFERENCES

[1] F. D'Errico, Micropitting Damage Mechanism on Hardened and Tempered, Nitrided, and Carburizing Steels, Materials and Manufacturing Processes 26(1) (2011) 7-13.

[2] H. Bhadeshia, Steels for bearings, Progress in Materials Science 57(2) (2012) 268-435.

[3] F. Sadeghi, B. Jalalahmadi, T.S. Slack, N. Raje, N.K. Arakere, A Review of Rolling Contact Fatigue, Journal of Tribology-Transactions of the Asme 131(4) (2009) 15.

[4] C. Santus, M. Beghini, I. Bartilotta, M. Facchini, Surface and subsurface rolling contact fatigue characteristic depths and proposal of stress indexes, Int J Fatigue 45 (2012) 71-81.

[5] Y. Ding, J.A. Gear, Spalling depth prediction model, Wear 267(5-8) (2009) 1181-1190.

[6] Y. Ding, N.F. Rieger, Spalling formation mechanism for gears, Wear 254(12) (2003) 1307-1317.

[7] J.A. Brandao, J.H.O. Seabra, J. Castro, Surface initiated tooth flank damage. Part II: Prediction of micropitting initiation and mass loss, Wear 268(1-2) (2010) 13-22.

[8] R.C. Dommarco, K.J. Kozaczek, P.C. Bastias, G.T. Hahn, C.A. Rubin, Residual stresses and retained austenite evolution in SAE 52100 steel under non-ideal rolling contact loading, Wear 257(11) (2004) 1081-1088.

[9] M.A. Moshier, B.M. Hillberry, The inclusion of compressive residual stress effects in crack growth modelling, Fatigue & Fracture of Engineering Materials & Structures 22(6) (1999) 519-526.

[10] S. Roy, S. Sundararajan, The effect of heat treatment routes on the retained austenite and Tribomechanical properties of carburized AISI 8620 steel, Surface & Coatings Technology 308 (2016) 236-243.

[11] J. Wei, A.Q. Zhang, P. Gao, A study of spur gear pitting under EHL conditions: Theoretical analysis and experiments, Tribology International 94 (2016) 146-154.

[12] S. Roy, J.N. Zhao, P. Shrotriya, S. Sundararajan, Effect of laser treatment parameters on surface modification and tribological behavior of AISI 8620 steel, Tribology International 112 (2017) 94-102.

[13] E.V. Zaretsky, Rolling bearing steels - a technical and historical perspective, Materials Science and Technology 28(1) (2012) 58-69.

[14] Y.B. Guo, M.E. Barkey, Modeling of rolling contact fatigue for hard machined components with process-induced residual stress, International Journal of Fatigue 26(6) (2004) 605-613.

[15] Q. Chen, G.T. Hahn, C.A. Rubin, V. Bhargava, The influence of residual-stresses on rolling-contact mode II driving force in bearing raceways, Wear 126(1) (1988) 17-30.

[16] Z.Z. Hu, M.L. Ma, Y.Q. Liu, J.H. Liu, The effect of austenite on low cycle fatigue in three-phase steel, Int J Fatigue 19(8-9) (1997) 641-646.

[17] I.V. Rivero, C.O. Ruud, Deviation of residual stress patterns in 52,100 bearing steel due to inherent microstructural transformations after rolling contact, Materials Characterization 53(5) (2004) 381-393.

[18] M. Abareshi, E. Emadoddin, Effect of retained austenite characteristics on fatigue behavior and tensile properties of transformation induced plasticity steel, Mater Design 32(10) (2011) 5099-5105.

[19] I. de Diego-Calderon, P. Rodriguez-Calvillo, A. Lara, J.M. Molina-Aldareguia, R.H. Petrov, D. De Knijf, I. Sabirov, Effect of microstructure on fatigue behavior of advanced high strength steels produced by quenching and partitioning and the role of retained austenite, Materials Science and Engineering a-Structural Materials Properties Microstructure and Processing 641 (2015) 215-224.

[20] C.L. Zheng, R. Dan, F.C. Zhang, B. Lv, Z.G. Yan, J. Shan, X.Y. Long, Effects of retained austenite and hydrogen on the rolling contact fatigue behaviours of carbide-free bainitic steel, Materials Science and Engineering a-Structural Materials Properties Microstructure and Processing 594 (2014) 364-371.

[21] V.F. da Silva, L.F. Canale, D. Spinelli, W.W. Bose, O.R. Crnkovic, Influence of retained austenite on short fatigue crack growth and wear resistance of case carburized steel, Journal of Materials Engineering and Performance 8(5) (1999) 543-548.

[22] A.P. Voskamp, R. Osterlund, P.C. Becker, O. Vingsbo, Gradual changes in residual-stress and microstructure during contact fatigue in ball-bearings, Metals Technology 7(JAN) (1980) 14-21.

[23] G. Totten, M. Howes, T. Inoue, Handbook of Residual Stress and Deformation of Steel, A S M International, Materials Park, United States, 2002.

[24] H.J. Kim, Y.G. Kweon, The effects of retained austenite on dry sliding wear behavior of carburized steels, Wear 193(1) (1996) 8-15.

[25] A.D. Jenson, S. Roy, S. Sundararajan, The evolution of hardness and tribofilm growth during running-in of case carburized steel under boundary lubrication, Tribology International 118 (2018) 1-10.

[26] K.L. Johnson, Contact mechanics, Cambridge University Press, Cambridge Cambridgeshire ; New York, 1985.

[27] A. Okabe, Spatial tessellations, Wiley Online Library1992.

[28] J.M. Melenk, I. Babuska, The partition of unity finite element method: Basic theory and applications, Computer Methods in Applied Mechanics and Engineering 139(1-4) (1996) 289-314.

[29] T. Belytschko, T. Black, Elastic crack growth in finite elements with minimal remeshing, International Journal for Numerical Methods in Engineering 45(5) (1999) 601-620.

[30] V. ABAQUS, 6.14 Documentation, Dassault Systemes Simulia Corporation, 2014.

[31] J.J.C. Remmers, R. de Borst, A. Needleman, The simulation of dynamic crack propagation using the cohesive segments method, Journal of the Mechanics and Physics of Solids 56(1) (2008) 70-92.

[32] 440C Martensitic Stainless Steel (UNS S44004). http://www.matweb.com/search/datasheet.aspx?matguid=850c5024f8d844af8ef95afab1a08792.

[33] AISI 8620 Steel, carburized, box cooled, reheated and double quenched, 150°C (300°F) temper, 13 mm (0.5 in.) round.

[34] J. Siepak, The Influence of Contact Stress on the Wear of a Carburized Steel Case with a High Content of Retained Austenite, Wear 80(3) (1982) 301-305.

[35] O. Asi, A.C. Can, J. Pineault, M. Belassel, The relationship between case depth and bending fatigue strength of gas carburized SAE 8620 steel, Surf Coat Tech 201(12) (2007) 5979-5987.

[36] Y. Shen, S.M. Moghadam, F. Sadeghi, K. Paulson, R.W. Trice, Effect of retained austenite - Compressive residual stresses on rolling contact fatigue life of carburized AISI 8620 steel, Int J Fatigue 75 (2015) 135-144.

[37] Z.J. Xie, Y.Q. Ren, W.H. Zhou, J.R. Yang, C.J. Shang, R.D.K. Misra, Stability of retained austenite in multi-phase microstructure during austempering and its effect on the ductility of a low carbon steel, Materials Science and Engineering a-Structural Materials Properties Microstructure and Processing 603 (2014) 69-75.

[38] G.N. Haidemenopoulos, A.T. Kermanidis, C. Malliaros, H.H. Dickert, P. Kucharzyk, W. Bleck, On the effect of austenite stability on high cycle fatigue of TRIP 700 steel, Materials Science and Engineering a-Structural Materials Properties Microstructure and Processing 573 (2013) 7-11.

[39] T. Giordani, T.R. Clarke, C.E.F. Kwietniewski, M.A. Aronov, N.I. Kobasko, G.E. Totten, Mechanical and Metallurgical Evaluation of Carburized, Conventionally and Intensively Quenched Steels, Journal of Materials Engineering and Performance 22(8) (2013) 2304-2313.

[40] M. Nygards, P. Gudmundson, Three-dimensional periodic Voronoi grain models and micromechanical FE-simulations of a two-phase steel, Computational Materials Science 24(4) (2002) 513-519.

[41] A. Bruckner-Foit, X.Y. Huang, Numerical simulation of micro-crack initiation of martensitic steel under fatigue loading, International Journal of Fatigue 28(9) (2006) 963-971.

[42] T. Slack, F. Sadeghi, Explicit finite element modeling of subsurface initiated spalling in rolling contacts, Tribology International 43(9) (2010) 1693-1702.

[43] P.S. Prevey, X-ray diffraction residual stress techniques, ASM International, ASM Handbook. 10 (1986) 380-392.

[44] J.H. Song, P.M.A. Areias, T. Belytschko, A method for dynamic crack and shear band propagation with phantom nodes, International Journal for Numerical Methods in Engineering 67(6) (2006) 868-893.

[45] T.M. Hatem, M.A. Zikry, Shear pipe effects and dynamic shear-strain localization in martensitic steels, Acta Materialia 57(15) (2009) 4558-4567.

[46] T.M. Hatem, M.A. Zikry, A model for determining initial dislocation-densities associated with martensitic transformations, Materials Science and Technology 27(10) (2011) 1570-1573.

[47] J.D. Verhoeven, Steel Metallurgy for the Non-Metallurgist, ASM International2007.

[48] M. Yaso, S. Hayashi, S. Morito, T. Ohba, K. Kubota, K. Murakami, Characteristics of Retained Austenite in Quenched High C-High Cr Alloy Steels, Mater Trans 50(2) (2009) 275-279.

[49] Standard Practice for X-Ray Determination of Retained Austenite in Steel with Near Random Crystallographic Orientation, ASTM E975-13.

[50] Bruker, TOPAS V4.2 User's Manual, 2009.

[51] X. Cheng, R. Petrov, L. Zhao, M. Janssen, Fatigue crack growth in TRIP steel under positive R-ratios, Engineering Fracture Mechanics 75(3-4) (2008) 739-749.

[52] K. Tanaka, Y. Akiniwa, Fatigue crack propagation behaviour derived from S-N data in very high cycle regime, Fatigue & Fracture of Engineering Materials & Structures 25(8-9) (2002) 775-784.